CHARACTERIZATION OF THE INFLUENCE OF ROTATIONAL AND TRAVERSE SPEEDS ON THE MECHANICAL AND MICROSTRUCTURAL PROPERTIES OF WIRES PRODUCED BY THE FSBE METHOD

P. Asadi,[a] M. Akbari,[b] O. Kohantorabi,[a] M. Peyghami,[c]   UDC 539.4
M. R. M. Aliha,[d,1] S. M. Salehi,[d,e] H. R. Asiabaraki,[b]
and F. Berto[f]

This study investigates the effects of tool traverse and rotational speeds in the friction stir back extrusion (FSBE) process on the microstructural and mechanical properties of brass wires produced. The microstructural properties were examined by microscopic tests and the mechanical properties of the wires by hardness and pressure tests. The material flow pattern, temperature history, and strain experienced by the materials were investigated using a numerical model to understand better the effects of tool traverse and rotational speed on the final properties of the wires. Numerical results showed that, on the one hand, the strain experienced by the material in the wire periphery is more than the center of the wire, and on the other hand, the material experiences a lower temperature in the wire periphery. The microstructural results showed that this more significant strain and lower temperature in the perimeter of the wires caused the grain size to be finer than the center of the wire. Moreover, a coarser microstructure is produced by a faster rotation speed or a slower traverse speed. Also, increasing the traverse speed or decreasing the rotational speed increased the hardness of wires produced, so that the sample made with a traverse and rotational speeds of 40 mm/min and 315 rpm had the highest hardness, and the wire made with a rotational speed of 800 rpm and a traverse speed of 25 mm/min had the lowest hardness.

Introduction. In recent years, many researchers have considered metal recycling due to the reduction of resources and the increased price of these metals [1]. Metals such as copper, aluminum, and their alloys are widely used for producing various parts. Among the significant scrap metals, there are metal chips produced during machining [2, 3]. Even though these wastes are generally filthy with cutting fluids and oils, the costs of cleaning them are far cheaper than the price of mining them. One of the most widely used methods for recycling these metals

---
[a]Department of Mechanical Engineering, Faculty of Engineering, Imam Khomeini International University, Qazvin, Iran. [b]Department of Mechanical Engineering, Technical and Vocational University (TVU), Tehran, Iran. [c]Department of Mechanical Engineering, Faculty of Engineering, Urmia University, Iran. [d]Welding and Joining Research Center, School of Industrial Engineering, Iran University of Science and Technology (IUST), Tehran, Iran ([1]mrm_aliha@iust.ac.ir). [e]School of Management, Economics and Progress Engineering, Iran University of Science and Technology, Tehran, Iran. [f]Department of Mechanical and Industrial Engineering, Norwegian University of Science and Technology (NTNU), Trondheim, Norway. Translated from Problemy Mitsnosti, No. 2, pp. 107 – 108, March – April, 2022. Original article submitted January 20, 2021.

is re-casting these chips [2, 4]. As a result, certain firms are required to collect the chips and transport them to the casting facilities, where they will be subjected to extrusion, rolling, and other operations in order to generate the final production. New recycling procedures, including friction stir back extrusion (FSBE), have evolved as a result of technological advancements, allowing businesses to recycle metal chips into extruded goods directly [5, 6].

Friction-based procedures, such as friction stir welding (FSW), have already proved their capacity to combine and mold materials in a solid state, resulting in products with specified mechanical characteristics [7–13]. A novel friction stirring approach was recently created with the goal of processing and recycling chips to produce bulk material. As a solid-state recycling method, the FSBE generates frictional heat to soften the metal chips, which are then combined and forced through a channel to form an integrated product such as a tube or wire by exerting sufficient pressure as a forging force [14, 15]. So far, research has been used to demonstrate the effectiveness of this method in recycling metal scrap. Lakshminarayanan et al. [15] devised a high-fidelity experimental approach for controlling essential FSBE process parameters for making high-strength ZE41 magnesium alloy tubes. They determined that the FSBE technique, in combined with carefully regulated process parameters, allows for the production of defect-free, high-strength ZE41 magnesium tubes with improved grain refinement. Mahmoodi et al. [16] produced the Al-SiC composite tube using a solid cylindrical AA7075 aluminum alloy bar and some SiC powder by the process of FSBE. They observed that SiC particles were almost distributed homogeneously among the aluminum phase. Alhourani et al. [17] investigated the effects of traverse speed and rotational speed on the mechanical characteristics, cycle duration, and power consumption of friction stir back extruded Mg AZ31-B tubes to find the best settings.

In previous works, only the mechanical and microstructural properties of the process have been investigated, and essential aspects of the process that affect the mechanical properties of the wires, such as the material flow pattern and temperature history, have not been adequately understood. Many aspects of the FSBE process, such as material flow pattern and material temperature and strain, cannot be investigated using experimental methods or are very difficult. FSBE process modeling is complicated due to the severe plastic deformation that occurs during the process, resulting in mesh distortion. Recent studies have shown that CEL can simulate severe plastic deformation (SPD) [18, 19]. Using the Eulerian formulation, it is possible to avoid significant mesh distortion during simulation. This method has recently been used to model manufacturing processes, especially processes with severe material deformation. Chen et al. [20] used the CEL technique to simulate dissimilar friction stir spot welding between aluminum and steel alloys. As well as showing the dispersion of materials at different dive depths, they also demonstrated hook formation during welding.

This research has studied the effects of tool traverse and rotation speed in the FSBE process on the mechanical and microstructural characteristics of brass wires produced. Also, the material flow pattern, temperature, and strain during the process were obtained by simulating the process. The simulation results helped to understand the microstructural properties and, consequently, the mechanical properties of the wires produced.

1. Experimental Procedure. Prior to using the FSBE method, a brass shaft with a height and diameter of 45 and 30 mm and the chemical composition stated in Table 1 was put into the matrix (mold cavity). The mold cavity was built of H13 hot-working steel that then heat-treated to a hardness of 52 RC (Fig. 1b). The FSBE tool was built of chrome-nickel steels with outer and inner diameters of 30 and 7 mm, respectively, and heat-treated to a hardness of 58 RC (Fig. 1a). The primary process parameters of rotation and traverse speeds of the tool were adjusted in this study to see how they affected the microstructural and mechanical properties of the brass wires produced. The rotation and traverse speed was adjusted between 315–800 rpm and 25–40 mm/min, respectively. The process setup and milling machine used to make the wires are illustrated in Fig. 2. The wires are cut, polished, and etched using a standard method for microstructural investigations under the optical microscope (OM).

The microhardness of the specimens was assessed using Vickers microhardness testing equipment at the center and the perimeter of the wire cross-section by applying a force of 200 g for 15 s. Cometech universal tensile/pressure test equipment was used to conduct the standard pressure test at ambient temperature with a strain rate of 10^{-3} s^{-1}. The pressure test specimens were in the length of 12 mm. The average microhardness and ultimate pressure strength (UPS) of the primary ingot were 100 HV and 500 MPa, respectively.

TABLE 1. Brass Chemical Compositions Utilized in This Investigation

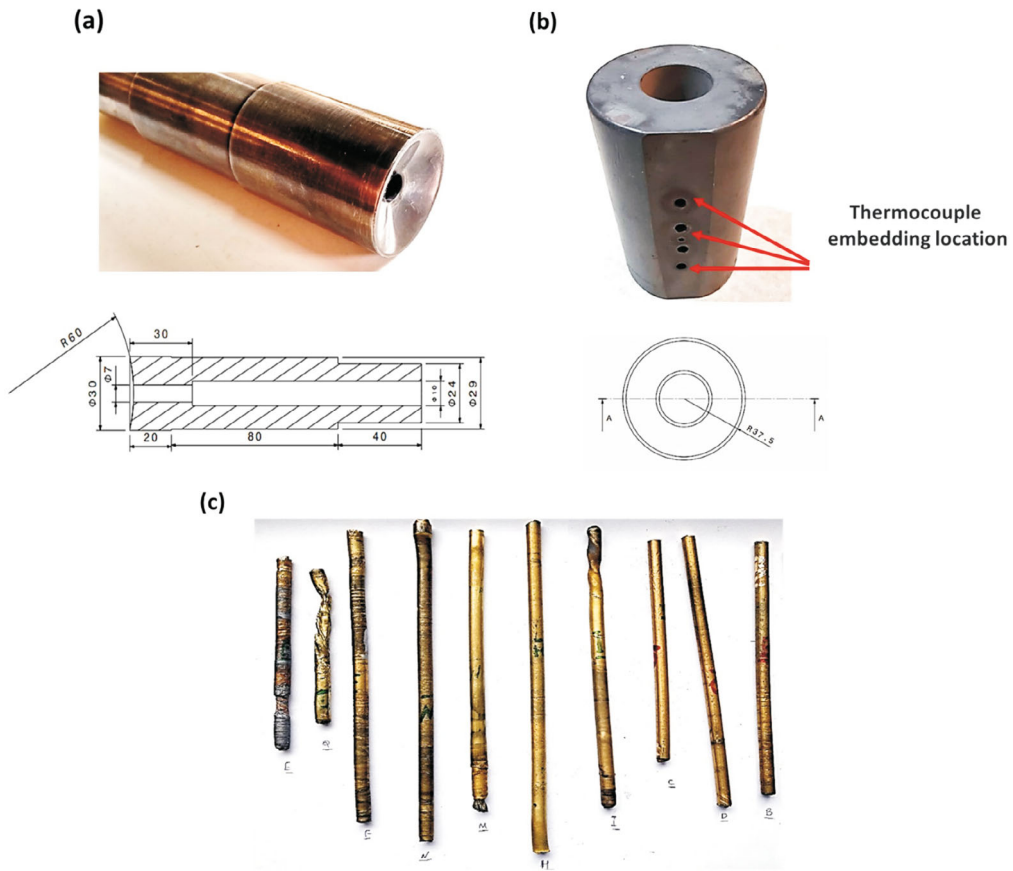| Element	Cu	Zn	Pb	Sn	Fe	Ni	Al	Mn	Si	S	P
wt.%	58.9	37.39	2.14	0.6	0.51	0.43	0.007	0.004	0.003	0.003	0.003

Fig. 1. (a) The tool with its dimensions; (b) the matrix with its dimensions; (c) image of some wires produced using the FSBE method.
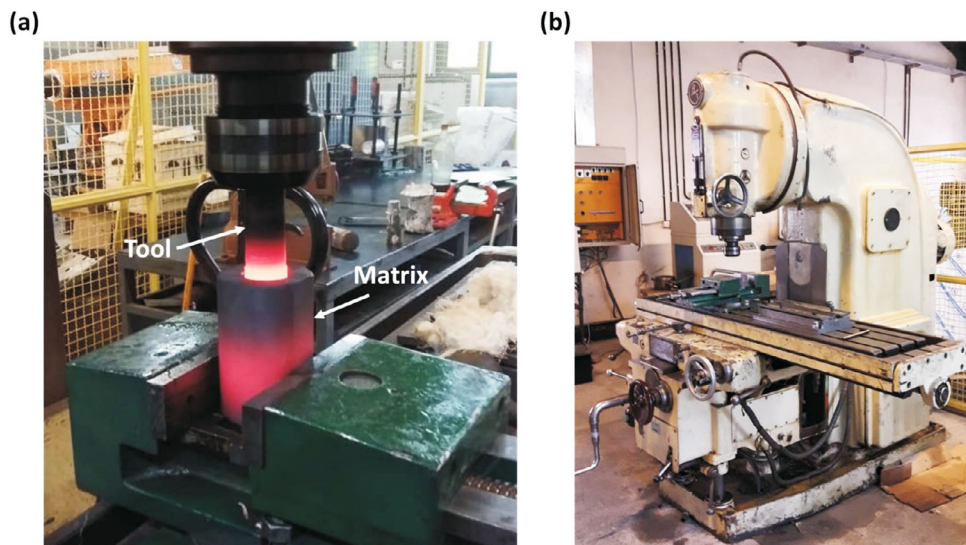

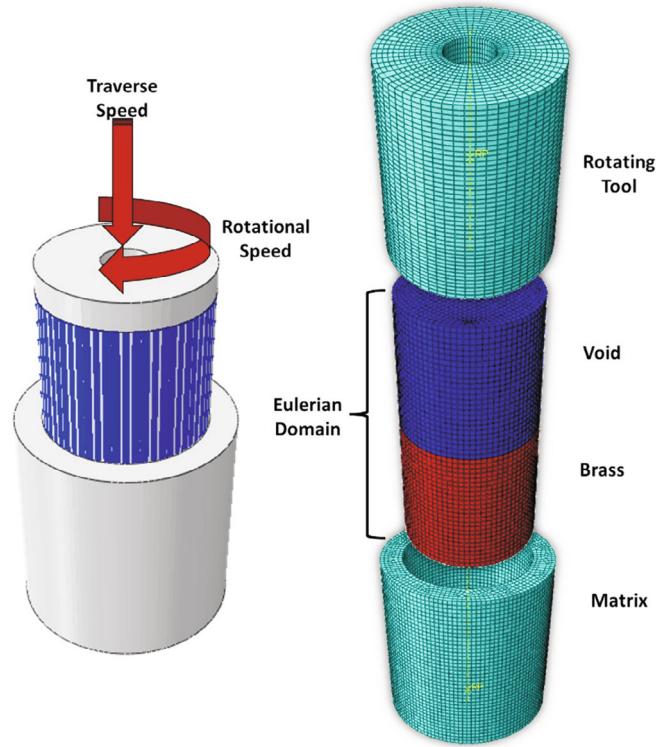Fig. 2. (a) The process setup; b) milling machine used to produce wires.

Fig. 3. The CEL model for FSBE.

2. Model Description. The temperature and strain history and flow of material during the FSBE of brass were simulated using the ABAQUS program. In this work, a CEL approach is used to replicate several elements of the process. The finite components are fixed in space in this technique, but the material may flow across them [21–24]. Consequently, the mesh distortion that is common in Lagrangian approaches is eliminated. The workpiece was treated as an Eulerian component having EC3D8RT elements, and the tool was treated as a rigid Lagrangian body (Fig. 3).

In FSBE, material flow stress is determined by strain, temperature, and strain rate. As a result, Johnson–Cook's (JC) material flow model for brass is utilized as follows:

$$\sigma = (A + B\varepsilon^n)\left[1 + C\ln\left(\frac{\dot{\varepsilon}}{\dot{\overline{\varepsilon}}}\right)\right]\left[1 - \left(\frac{T - T_r}{T_m - T_r}\right)^m\right], \tag{1}$$

where A, B, C, n, and m are constants related to the material, T_r is the ambient temperature, T_m is melting temperature, $\dot{\overline{\varepsilon}}$ is the normalizing strain rate, ε represents the plastic strain, and $\dot{\varepsilon}$ is the effective plastic strain rate. Table 2 shows the Johnson–Cook parameters for brass alloys [12].

A convective heat transfer coefficient is utilized to model natural convection heat loss at the mold cavity and tool outer surfaces. Using general contact interaction, all contact points between workpiece and tool were considered. Moreover, the penalty equation and the hard contact pressure enclosure modeled the tangential and normal contact to minimize the penetration of workpiece nodes into the tool. Therefore, it is possible to find the compressive stress at the interface. The tool/workpiece contact has been defined using a general contact formulation [26].

A thermometer was utilized to record the temperature history throughout the process. The thermocouple was put into the holes in the mold cavity body. The experimental and simulation thermal history curves are compared to ensure model accuracy (Fig. 4). Temperatures are taken on the mold cavity body at a distance of 3 mm from the inner cylindrical surface and 10 mm from the top surface. As can be seen, the experimental and numerical findings are in

TABLE 2. JC Model Constants for Brass Alloys [25]

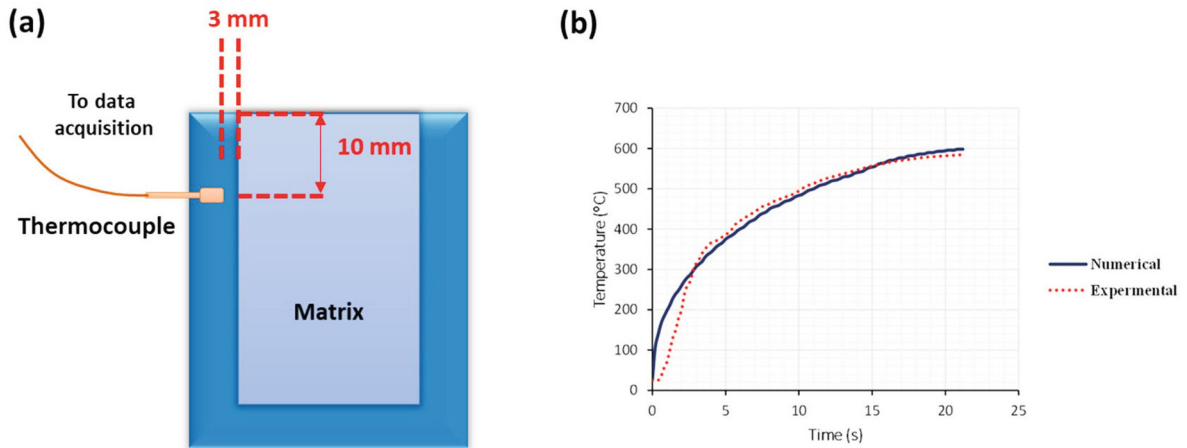| Material	A (MPa)	B (MPa)	C	n	m
Brass	112	505	0.009	0.42	1.68

Fig. 4 (a) Position of the thermocouple inside the matrix; (b) the numerical and experimental temperature history curves.

perfect accord. Although the highest temperature in the mold cavity reaches over 600℃, the temperature at the tool/workpiece contact is substantially higher.

3. Results and Discussion.

3.1. Temperature and Strain Distribution. Figure 5 illustrates the distribution of temperature acquired for the workpieces under process by various tool traverse and rotational speeds. The heat required to soften the material in the FSBE process is mainly provided by the friction between the tool and the material [27–30]. Also, some heat is generated due to plastic deformation during the process, which increases the total heat produced in the material [31]. This heat softens the material by raising the temperature of the workpiece to 60–95% of the melting point of the substance [32–35]. The tool is then moved axially to deform the material and decrease its diameter. The heat generated due to the plastic deformation, similar to the frictional heat generated, has the highest value at the interface. As a result, the peak temperature appears in the interface. Also, the temperature in the periphery of the wires being produced is lower than the center of these wires. Heat transfer between the surface of the wires and the tool reduces the temperature in this area.

Figure 5 depicts the influence of tool rotational and traverse speeds on temperature distribution. As the tool's traverse speed increases, the maximum material temperature decreases during the process (Fig. 5). On the other hand, reducing the rotational speed of the tool from 800 to 600 rpm has reduced the heat produced, and as a result, the temperature in the material has decreased. Reducing the rotation speed reduces plastic deformation and frictional heat generation. It may be determined by comparing the peak temperature attained in various input parameters that samples with a greater rotation speed to traverse speed ratio (ω/v) have a higher peak temperature.

Besides the maximum temperature and thermal cycle, an under-processed material experiences plastic deformation aspects, such as strain rate and effective strain, which influence the wire microstructure and, as a consequence, influence mechanical properties [36–38]. Furthermore, during friction-stir-based procedures, the amount of strain imparted to the material is substantially larger than during other severe plastic deformation (SPD) methods [39]. Figure 6 illustrates the strain distribution on the surface of the wires being produced. As it is known, with increasing the rotational speed or decreasing the traverse speed of the tool, the strain experienced by the material increases, which indicates an increase in the intensity of the material flow. Moreover, due to the increased linear velocity of the tool at the wire perimeter rather than the tool center, the materials at the wire periphery incur more strain (Fig. 6).
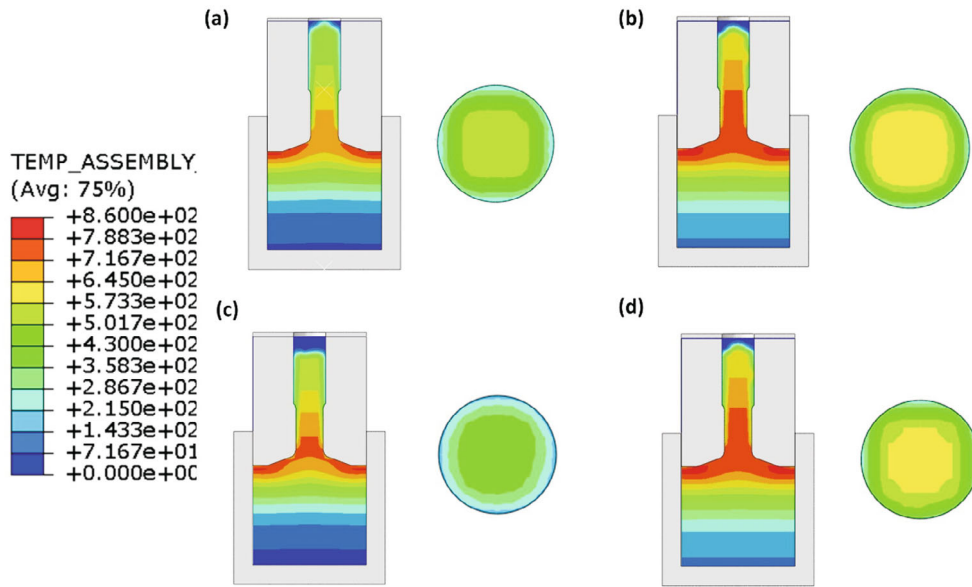
Fig. 5. The distribution of temperature during the process by various tool rotational and traverse speeds of 800 rpm and 40 mm/min (a), 800 rpm and 25 mm/min (b), 600 rpm and 40 mm/min (c), and 600 rpm and 25 mm/min (d).
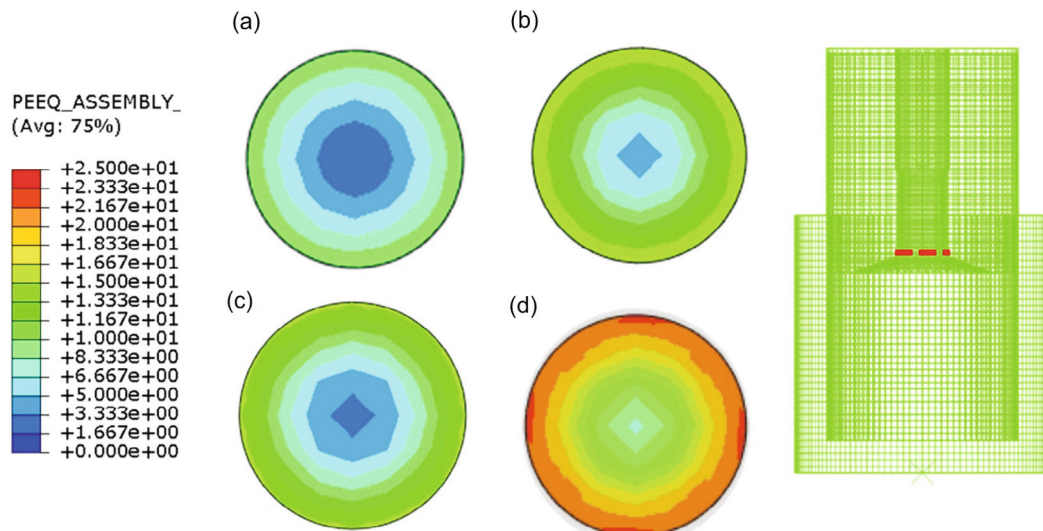

Fig. 6. The strain distribution of the wires produced by different tool rotational and traverse speeds of 600 rpm and 40 mm/min (a), 600 rpm and 25 mm/min (b), 800 rpm and 40 mm/min (c), 800 rpm and 25 mm/min (d).

3.2. Forces. The forces acting on the tool are critical parameters in the manufacturing process that determine the life of the tool and, therefore, production costs [34, 36, 40]. The forces that the tool experiences in FSBE are much higher than in other friction-based processes due to the large diameter of the tool as well as the high penetration of the tool shoulder into the material. A tool in FSBE processing experiences axial forces. The tool is confronted with an axial force that tends to elevate it as it plunges through the workpiece. The axial force is unavoidable due to the need to keep the tool on the workpiece surface.

Figure 7 shows the effect of the traverse and rotational speed of the tool on the axial force applied to the tool. By increasing the rotational speed, the amount of heat produced and, as a result, the temperature in the
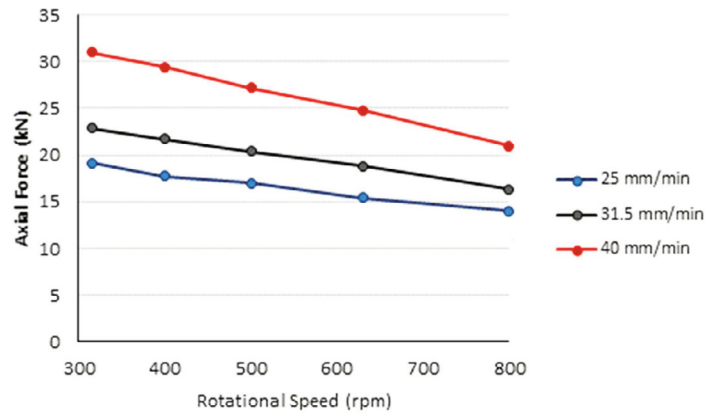
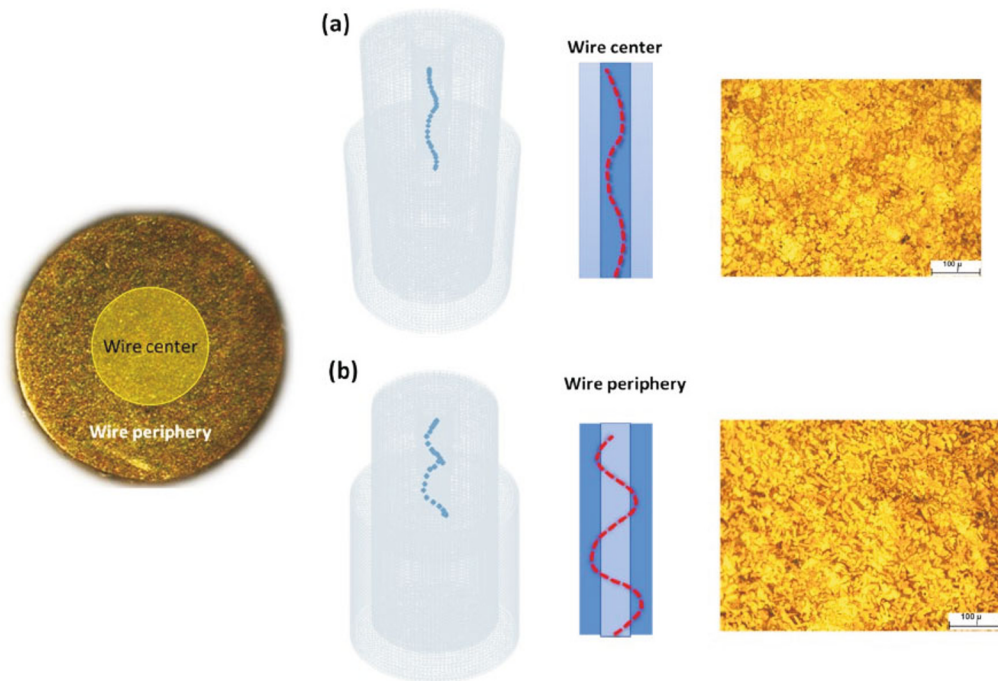Fig. 7. The effect of rotational and traverse speed on force.

Fig. 8. Material flow and microstructural behavior in two areas: the center (a) and periphery (b) of the produced samples.

workpiece increases, which causes the materials under the process to become more softened. Softening of materials with increasing temperature improves material flow and thus reduces the force applied to the tool. As the tool progresses faster, the materials spend less time under frictional heat and, as observed, experience lower temperatures. Decreasing the temperature by increasing the advancing speed of the tool reduces the softening of the material and thus increases the force on the tool.

3.3. Microstructure of Wires. Figure 8 illustrates the central and peripheral microstructures of the cross-section of the brass wires produced at various process settings. Both samples have a finer perimeter microstructure than the center microstructure. This disparity is connected to the strain and the temperature experienced, both of which have an impact on microhardness [37].

The materials at the wire periphery are subjected to additional strain due to the tool's increased linear velocity at the wire perimeter rather than the tool center (Fig. 6). Increased strain lowers grain size in the produced microstructure by increasing nucleation sites over the recrystallization process, which is well known.
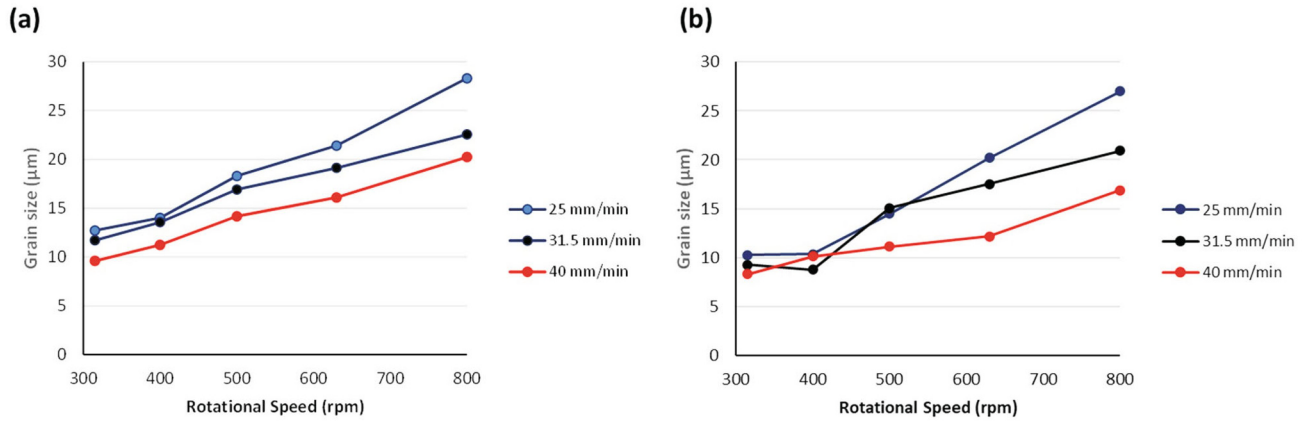
324

Fig. 9 Variation of the grain size at the wire center (a) and wire periphery (b).

In terms of temperature over time, it may be said that the FSBE tool's surface functions as a heat sink, cooling the outer surface of the wires in contact with the tool, resulting in a lower temperature at the wires' surface than at the wires' core (Fig. 5). As a consequence of the lower temperature at the wire's edge, grain development is reduced throughout the operation. The smaller grain size in this location is due to higher strain and lower temperature on the outer surface of the wires.

In order to better understand the difference between the microstructure in the periphery and center of the wires produced, the material flow in these two areas was modeled. In the original stock, the points are 1 and 3 mm from the center axis (see Fig. 8). From 3D and front views, their routes through the FSBE from initial feedstock to final wire produced may be seen. As can be observed, from the starting stock to the size channel, where the wire is formed, all points spin around the axis and climb in a virtually helical manner. The path for the point in the center zone, on the other hand, is almost entirely helical and moves practically vertically at a slower rate. The path is a conical helix for the point at the wire's periphery, and it takes an inward spiral movement in addition to upward movement. Therefore, it must follow the longer path at a higher speed. As a result, as previously stated, a greater strain is applied to the points near the wire's periphery. The higher the strain, the higher the dislocation density and the more favorable sites for grain nucleation, resulting in a microstructure with more refined grains.

Figure 9 demonstrates the influence of traverse and rotational speed on grain size. Although the amount of strain applied to the materials is reduced by increasing the traverse speed (Fig. 9), temperature drop appears to be more effective than strain reduction because by increasing the plunge speed, the grain size is reduced at the periphery and center of the wires. In addition to the temperature decrease, increasing the traverse speed minimizes the duration of the material exposure to higher temperatures, which helps avoid grain development. Moreover, the grain size is lowered by lowering the rotation speed from 800 to 315 rpm. In general, when the process parameters, including traverse and rotational speed, are changed, temperature becomes the most critical factor in determining grain size.

3.4. Mechanical Properties of the Wires. The fluctuation of microhardness versus tool traverse and rotational speeds is shown in Fig. 10. The hardness of the samples is increased by raising the traverse speed or reducing the rotation speed. According to the Hall–Petch equation, the hardness of alloys is affected by grain size, and hardness rises as grain size decreases [41]. The general face of the Hall–Petch relation is as Eq. (2), in which A, k, and α can be estimated for an alloy through several samples by varying the grain size and hardness. Equation (3) is extracted for the relationship between the grain size and hardness of the brass wire samples produced by FSBE in this study and can predict the hardness of the sample closely through its grain size. Therefore, the values for A, k, and α are 70, 218, and 0.5, respectively.

$$HV = A + kd^{-\alpha}, \tag{2}$$

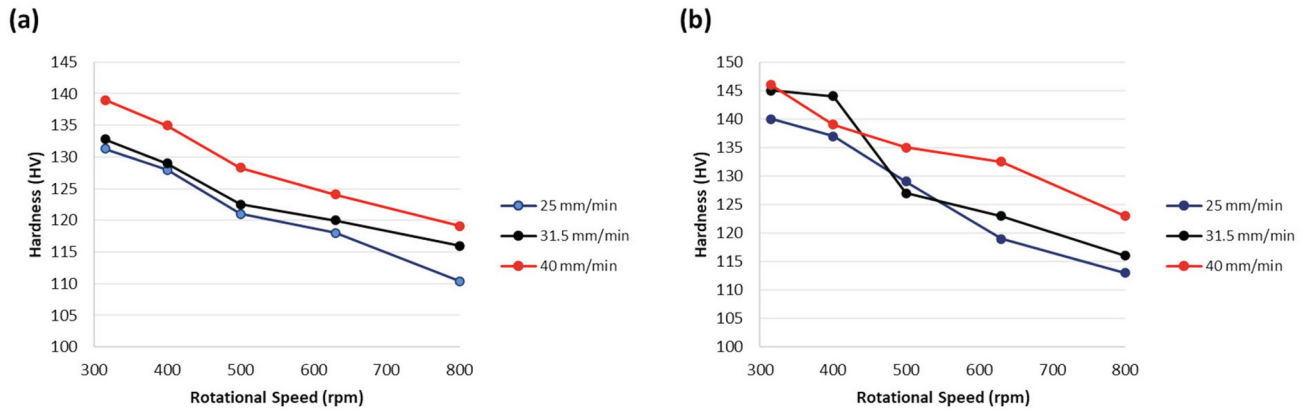$$HV = 70 + 218d^{-0.5}. \tag{3}$$

325

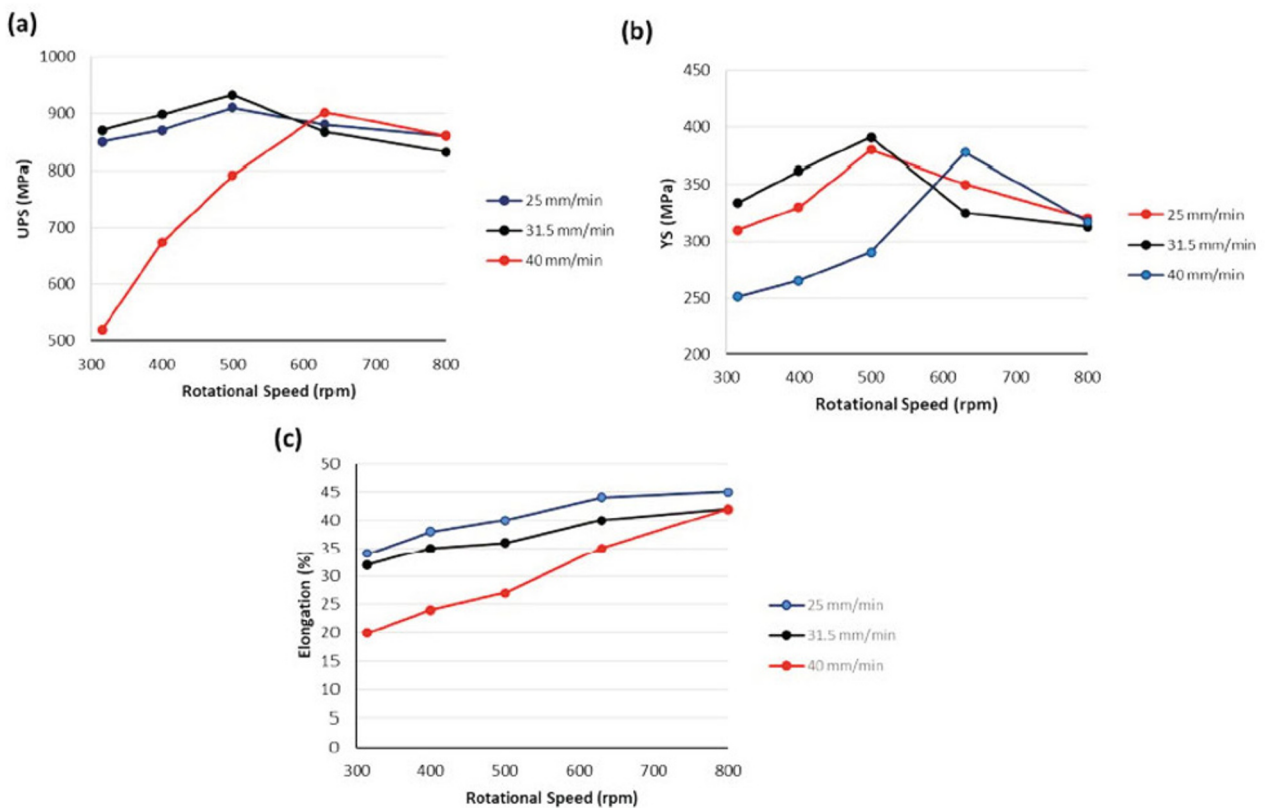Fig. 10 Hardness variation at the wire center (a) and wire periphery (b).

Fig. 11. The effect of rotational and traverse speed on UPS (a), yield stress (b), and elongation (c) of the wires.

Figure 11a shows the UPS vs. tool rotation and traverse speeds variation curves. When it comes to the input parameters, UPS operates differently than when it comes to the grain size and hardness of the samples. A factor other than temperature and strain seems to impact the UPS of the samples. Despite the fact that a material's microstructure and hardness dictate its strength, macrostructure discontinuities induced by insufficient flow of material during the FSBE mainly influence the UPS in the samples produced.

It is expected that the UPS, similar to the hardness, should be raised as the temperature and grain size are reduced. The traverse speed changed between 25 and 40 mm/min, and it is expected that by increasing the traverse speed and decreasing the grain size and temperature, which improves the hardness, the UPS shows an improvement.
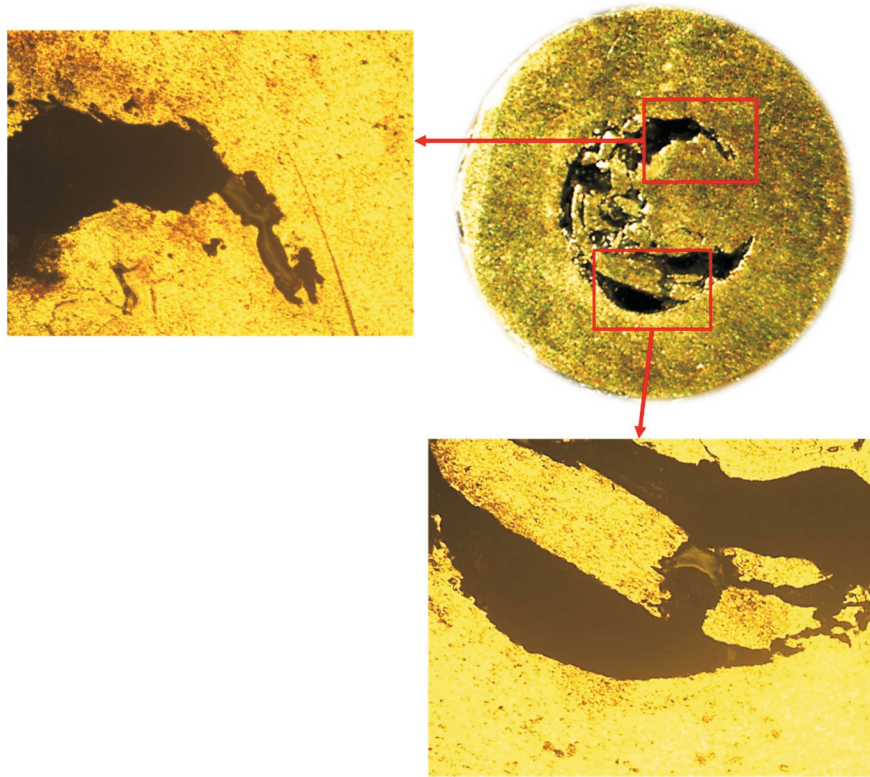
Fig. 12. The defects generated in the cross-section of the wires produced with the traverse speed of 40 mm/min and the rotational speed of 315 rpm.

However, paying attention to the UPS variation curves in Fig. 11a, it can be concluded that there is no clear trend for the effects of traverse speed on the UPS; this is due to some defects that may emerge in the sample inside.

Figure 12 illustrates the defect that emerged in the center of the generated sample at a traverse speed of 40 mm/min, which indicates inadequate heat generation results in poor formability of the materials in the process. Actually, the absence of heat causes insufficient material softening, leading to poor under-process material flow (strain). Consequently, the produced wire UPS is substantially dropped as a consequence of this major fault.

Reversal behavior is also seen in the effect of rotational speed on the UPS. As noted, increasing the rotational speed reduced microhardness; hence, wire produced at a higher rotation speed should have a lower UPS. To show this behavior, the rotational speed increased from 500 to 800 rpm, which lowered the UPS. The rotational speed of 315 rpm, on the other hand, resulted in the lowest UPS. Similarly, the wire's cross-section flaw resulted in this much-reduced UPS. Therefore, there is an optimum value for rotational speed in a constant traverse speed which provides the highest UPS. While in the higher rotational speeds (than the optimum speed), the UPS is reduced due to the higher temperature and excessive softening and, on the other side, the reduction of rotational speeds decreases the UPS again due to the formation of defects as the result of poor flow of inadequately heated (softened) materials.

Although the slope of variation curves is slightly different for yield strength, the general behavior is similar to that of the UPS (Fig. 11b). Concerning the elongation of the samples before the fracture (Fig. 11c), the elongation is lower for the samples produced with lower rotational speed and involves defects. Therefore, for the samples produced with rotational speeds between 315–630 rpm, the rotational speed increase results in an increase in the elongation as well. However, beyond 630 rpm, which was the optimum rotational speed for UPS and YS, the elongation increases with rotational speed. Actually, the elongation can be improved by softening the material regardless of strength. Thus, in the range of 315–630 rpm, the elongation is improved as the result of both elimination of defects and softening of material and increasing the grain size; however, after elimination of defects, just material softening by rotational speed increase has improved the sample elongation.

Conclusions. In this research, the effects of the rotational and linear velocity of the tool on the microstructural and mechanical properties of brass wires produced using the FSBE method are investigated. In order to investigate the effects of process parameters, the material flow pattern, thermal history, and strain experienced by the materials were obtained using process simulations. Experiments were used to validate a CEL model constructed using the ABAQUS program. The findings reveal that:

1. The maximum temperature and strain occur near the tool/workpiece contact but farther away from the tool axis. The strain and temperature that the material experiences throughout the process rise as the rotation speed or traverse speed increases.

2. The microstructure of a generated FSBE sample (wire) is finer in the perimeter than in the middle of the cross-section.

3. A coarser microstructure will emerge from a greater rotational to traverse speed ratio.

4. The pattern of material flow during the process is conical helix and is unaffected by process parameters.

5. Raising the traverse speed or lowering the rotation speed increases the sample hardness.

6. The UPS of the samples seems to be influenced by a component other than temperature and strain. Although the microstructure and hardness of a material determine its strength, macrostructure discontinuities caused by inadequate flow of material during the FSBE process have a major impact on the UPS in the samples generated.

REFERENCES

1. G. Jamali, S. Nourouzi, and R. Jamaati, "Microstructure and mechanical properties of AA6063 aluminum alloy wire fabricated by friction stir back extrusion (FSBE) process," *Int. J. Min. Met. Mater.*, **26**, No. 8, 1005–1012, (2019), https://doi.org/10.1007/s12613-019-1806-9.

2. P. Asadi and M. Akbari, "Numerical modeling and experimental investigation of brass wire forming by friction stir back extrusion," *Int. J. Adv. Manuf. Technol.*, **116**, 3231–3245 (2021), https://doi.org/10.1007/s00170-021-07729-5.

3. M. Paidar, V. Mohanavel, O. O. Ojo, et al., "Dieless Friction Stir Extrusion-Brazing (DFSE-B) of AA2024-T3 aluminum alloy to Copper with Zn interlayer," *Results Phys.*, **24**, 104101 (2021), https://doi.org/10.1016/j.rinp.2021.104101.

4. M. Akbari and P. Asadi, "Optimization of microstructural and mechanical properties of brass wire produced by friction stir extrusion using Taguchi method," *P. I. Mech. Eng. L-J. Mat.*, **235**, No. 12, 2709–2719 (2021), https://doi.org/10.1177/14644207211032992.

5. V. C. Shunmugasamy, E. Khalid, and B. Mansoor, "Friction stir extrusion of ultra-thin wall biodegradable magnesium alloy tubes — Microstructure and corrosion response," *Mater. Today Commun.*, **26**, 102129 (2021), https://doi.org/10.1016/j.mtcomm.2021.102129.

6. G. Jamali, S. Nourouzi, and R. Jamaati, "Manufacturing of gradient Al/SiC composite wire by friction stir back extrusion," *CIRP J. Manuf. Sci. Technol.*, **35**, 735–743 (2021), https://doi.org/10.1016/j.cirpj.2021.09.004.

7. A. Yazdipour and A. Heidarzadeh, "Effect of friction stir welding on microstructure and mechanical properties of dissimilar Al 5083-H321 and 316L stainless steel alloy joints," *J. Alloy. Compd.*, **680**, 595–603 (2016), https://doi.org/10.1016/j.jallcom.2016.03.307.

8. O. M. Jarrah, M. A. Nazzal, and B. M. Darras, "Numerical modeling and experiments of Friction Stir Back Extrusion of seamless tubes," *CIRP J. Manuf. Sci. Technol.*, **31**, 165–177 (2020), https://doi.org/10.1016/j.cirpj.2020.11.001.

9. Z. S. Mousavi, S. Karimi, A. Heidarpour, et al., "Microstructural variation and corrosion behavior of 60/40 brass/Ti$_2$SC surface composite through friction stir processing," *J. Mater. Eng. Perform.*, **31**, 3445–3456 (2022), https://doi.org/10.1007/s11665-021-06441-5.

10. H. Bang, H. Bang, J. H. Hong, et al., "Effect of tungsten-inert-gas preheating on mechanical and microstructural properties of friction stir welded dissimilar Al alloy and mild steel," *Strength Mater.*, **48**, No. 1, 152–159 (2016), https://doi.org/10.1007/s11223-016-9750-7.

11. Y. C. Zhang, Z. H. Ren, X. W. Kong, et al., "Thermal-fluid coupling numerical simulation of axial ultrasonic vibration friction stir welding," *Strength Mater.*, **51**, No. 6, 908–916 (2019), https://doi.org/10.1007/s11223-020-00141-6.

12. M. R. M. Aliha, M. Shahheidari, M. Bisadi, et al., "Mechanical and metallurgical properties of dissimilar AA6061-T6 and AA7277-T6 joint made by FSW technique," *Int. J. Adv. Manuf. Technol.*, **86**, No. 9, 2551–2565 (2016), https://doi.org/10.1007/s00170-016-8341-x.

13. M. R. M. Aliha, S. M. N. Ghoreishi, D. M. Imani, et al., "Mechanical and fracture properties of aluminium cylinders manufactured by orbital friction stir welding," *Fatigue Fract. Eng. Mater. Struct.*, **43**, No. 7, 1514–1528 (2020), https://doi.org/10.1111/ffe.13229.

14. A. Djerida, Z. Zhao, and J. Zhao, "Robust background generation based on an effective frames selection method and an efficient background estimation procedure (FSBE)," *Signal Process.-Image*, **78**, 21–31 (2019), https://doi.org/10.1016/j.image.2019.06.001.

15. A. K. Lakshminarayanan, S. Ramachandran, B. Rajabharathi, and W. Mirihanage, "Decisive influence of critical process parameters on the microstructure and tensile properties of friction stir back extruded magnesium alloy tubes," *J. Manuf. Process.*, **73**, 207–219 (2022), https://doi.org/10.1016/j.jmapro.2021.11.013.

16. M. Mahmoodi, K. Tahmasbi, and M. Zaroodi, "Microstructure and mechanical characterization of Al–SiC MMC tube produced via friction stir back extrusion," *Trans. Indian Inst. Met.*, **74**, No. 11, 2609–2620 (2021), https://doi.org/10.1007/s12666-021-02325-3.

17. A. Alhourani, M. Awad, M. A. Nazzal, and B. M. Darras, "Optimization of friction stir back extrusion mechanical properties and productivity of magnesium AZ31-B seamless tubes," *P. I. Mech. Eng.-B J. Eng.*, **235**, No. 13, 2143–2154 (2021), https://doi.org/10.1177/09544054211014465.

18. M. Grujicic, J. S. Snipes, S. Ramaswami, et al., "Computational analysis of the intermetallic formation during the dissimilar metal aluminum-to-steel friction stir welding process," *P. I. Mech. Eng.-L J. Mat.*, **233**, No. 6, 1080–1100 (2017), https://doi.org/10.1177/1464420716673670.

19. Q. Chu, X. W. Yang, W. Y. Li, et al., "Numerical analysis of material flow in the probeless friction stir spot welding based on Coupled Eulerian-Lagrangian approach," *J. Manuf. Process.*, **36**, 181–187 (2018), https://doi.org/10.1016/j.jmapro.2018.10.013.

20. K. Chen, X. Liu, and J. Ni, "Thermal-mechanical modeling on friction stir spot welding of dissimilar materials based on Coupled Eulerian-Lagrangian approach," *Int. J. Adv. Manuf. Technol.*, **91**, No. 5, 1697–1707 (2017), https://doi.org/10.1007/s00170-016-9884-6.

21. M. Akbari and P. Asadi, "Dissimilar friction stir lap welding of aluminum to brass: Modeling of material mixing using coupled Eulerian–Lagrangian method with experimental verifications," *P. I. Mech. Eng.-L J. Mat.*, **234**, No. 8, 1117–1128 (2020), https://doi.org/10.1177/1464420720922560.

22. M. Akbari, P. Asadi, and R. A. Behnagh, "Modeling of material flow in dissimilar friction stir lap welding of aluminum and brass using coupled Eulerian and Lagrangian method," *Int. J. Adv. Manuf. Technol.*, **113**, No. 3, 721–734 (2021), https://doi.org/10.1007/s00170-020-06541-x.

23. P. Asadi and M. Akbari, "Numerical modeling and experimental investigation of brass wire forming by friction stir back extrusion," *Int. J. Adv. Manuf. Technol.*, **116**, No. 9, 3231–3245 (2021), https://doi.org/10.1007/s00170-021-07729-5.

24. P. Asadi, M. Mirzaei, and M. Akbari, "Modeling of pin shape effects in bobbin tool FSW," *Int. J. Lightweight Mater. Manuf.*, **5**, No. 2, 162–177 (2022), https://doi.org/10.1016/j.ijlmm.2021.12.001.

25. K. M. Tse, T. Long Bin, B. Yang, et al., "Effect of helmet liner systems and impact directions on severity of head injuries sustained in ballistic impacts: a finite element (FE) study," *Med. Biol. Eng. Comput.*, **55**, (2016), https://doi.org/10.1007/s11517-016-1536-3.

26. D. Das, S. Bag, and S. Pal, "A finite element model for surface and volumetric defects in the FSW process using a coupled Eulerian–Lagrangian approach," *Sci. Technol. Weld. Joi.*, **26**, No. 5, 412–419 (2021), https://doi.org/10.1080/13621718.2021.1931760.

27. M. R. M. Aliha, M. H. Kalantari, S. M. N. Ghoreishi, et al., "Mixed mode I/II crack growth investigation for bi-metal FSW aluminum alloy AA7075-T6/pure copper joints," *Theor. Appl. Fract. Mech.*, **103**, 102243 (2019), https://doi.org/10.1016/j.tafmec.2019.102243.

28. O. Ikumapayi, E. Akinlabi, A. Sharma, et al., "Tribological, structural and mechanical characteristics of friction stir processed aluminium-based matrix composites reinforced with stainless steel micro-particles," *Eng. Solid Mech.*, **8**, No. 3, 253–270 (2020), https://doi.org/10.5267/j.esm.2019.12.001.

29. S. Narasimharaju and S. Sankunny, "Microstructure and fracture behavior of friction stir lap welding of dissimilar AA 6060-T5/pure copper," *Eng. Solid Mech.*, **7**, No. 3, 217–228 (2019), https://doi.org/10.5267/j.esm.2019.5.002.

30. M. Lemi, E. Gutema, and M. Gopal, "Modeling and simulation of friction stir welding process for AA6061-T6 aluminum alloy using finite element method," *Eng. Solid Mech.*, **10**, No. 2, 139–152 (2022), https://doi.org/10.5267/j.esm.2022.2.001.

31. U. Acharya, M. K. Yadava, A. Banik, et al., "Effect of heat input on microstructure and mechanical properties of friction stir welded AA6092/17.5 SiCp-T6," *J. Mater. Eng. Perform.*, **30**, No. 12, 8936–8946 (2021), https://doi.org/10.1007/s11665-021-06122-3.

32. I. Dinaharan, S. Zhang, G. Chen, and Q. Shi, "Titanium particulate reinforced AZ31 magnesium matrix composites with improved ductility prepared using friction stir processing," *Mater. Sci. Eng. A*, **772**, 138793 (2020), https://doi.org/10.1016/j.msea.2019.138793.

33. I. Dinaharan, R. Thirunavukkarasu, N. Murugan, and E. T. Akinlabi, "Microstructure evolution and tensile behavior of dissimilar friction stir-welded pure copper and dual-phase brass," *Metallogr., Microstruct. Anal.*, **8**, No. 5, 735–748 (2019), https://doi.org/10.1007/s13632-019-00579-4.

34. M. Akbari, M. R. M. Aliha, S. M. E. Keshavarz, and A. Bonyadi, "Effect of tool parameters on mechanical properties, temperature, and force generation during FSW," *P. I. Mech. Eng.-L J. Mat.*, **233**, No. 6, 1033–1043 (2016), https://doi.org/10.1177/1464420716681591.

35. F. Taheri-Behrooz, M. R. M. Aliha, M. Maroofi, and V. Hadizadeh, "Residual stresses measurement in the butt joint welded metals using FSW and TIG methods," *Steel Compos. Struct.*, **28**, 759–766 (2018), https://doi.org/10.12989/scs.2018.28.6.759.

36. M. Akbari, A. Khalkhali, S. M. E. Keshavarz, and E. Sarikhani, "The effect of in-process cooling conditions on temperature, force, wear resistance, microstructural, and mechanical properties of friction stir processed A356," *P. I. Mech. Eng.-L J. Mat.*, **232**, No. 5, 429–437 (2016), https://doi.org/10.1177/1464420716630569.

37. M. Akbari, A. Khalkhali, S. M. E. Keshavarz, and E. Sarikhani, "Investigation of the effect of friction stir processing parameters on temperature and forces of Al–Si aluminum alloys," *P. I. Mech. Eng.-L J. Mat.*, **232**, No. 3, 213–229 (2015), https://doi.org/10.1177/1464420715621337.

38. M. Akbari and P. Asadi, "Optimization of microstructural and mechanical properties of friction stir welded A356 pipes using Taguchi method," *Mater. Res. Express*, **6**, No. 6, 066545 (2019), https://doi.org/10.1088/2053-1591/ab0d72.

39. P. Asadi, M. Akbari, and H. Karimi-Nemch, *Simulation of Friction Stir Welding and Processing*, in: M. K. B. Givi and P. Asadi (Eds.), *Advances in Friction-Stir Welding and Processing*, Woodhead Publishing (2014), pp. 499–542.

40. K. K. Ramachandran and N. Murugan, "Influence of axial force on tensile strength and microstructural characteristics of friction stir butt-welded aluminum alloy/steel joints," *Strength Mater.*, **51**, No. 2, 300–316 (2019), https://doi.org/10.1007/s11223-019-00076-7.

41. T. Huang, L. Shuai, A. Wakeel, et al., "Strengthening mechanisms and Hall–Petch stress of ultrafine grained Al-0.3%Cu," *Acta Mater.*, **156**, 369–378 (2018), https://doi.org/10.1016/j.actamat.2018.07.006.